remote sensing

MDPI

Article

Real-Time Tsunami Detection with Oceanographic Radar Based on Virtual Tsunami Observation Experiments

Kohei Ogata [1], Shuji Seto [2], Ryotaro Fuji [1,3], Tomoyuki Takahashi [4] and Hirofumi Hinata [1,*]

[1] Department of Civil and Environmental Engineering, Faculty of Engineering, Ehime University, 3 Bunkyo-cho, Matsuyama, Ehime 790-8577, Japan; ogata.kohei.13@cee.ehime-u.ac.jp (K.O.); ryotaro_fuji@kk-grp.jp (R.F.)

[2] International Research Institute of Disaster Science and Core Research Cluster of Disaster Science, Tohoku University, 468-1 Aramaki Aza Aoba, Aoba-ku, Sendai, Miyagi 980-8572, Japan; setosh@irides.tohoku.ac.jp

[3] Technology Management Department, Kokusai Kogyo Co., Ltd., 2-24-1 Harumi-cho, Fuchu, Tokyo 183-0057, Japan

[4] Faculty of Safety Science, Kansai University, 7-1 Hakubai-cho, Takatsuki, Osaka 569-1098, Japan; tomot@kansai-u.ac.jp

* Correspondence: hinata.hirofumi.dv@ehime-u.ac.jp; Tel.: +81-89-927-9835

Received: 12 June 2018; Accepted: 13 July 2018; Published: 17 July 2018

Abstract: The tsunami generated by the 2011 Tohoku-Oki earthquake was the first time that the velocity fields of a tsunami were measured by using high-frequency oceanographic radar (HF radar) and since then, the development of HF radar systems for tsunami detection has progressed. Here, a real-time tsunami detection method was developed, based on virtual tsunami observation experiments proposed by Fuji et al. In the experiments, we used actual signals received in February 2014 by the Nagano Japan Radio Co., Ltd. radar system installed on the Mihama coast and simulated tsunami velocities induced by the Nankai Trough earthquake. The tsunami was detected based on the temporal change in the cross-correlation of radial velocities between two observation points. Performance of the method was statistically evaluated referring to Fuji and Hinata. Statistical analysis of the detection probability was performed using 590 scenarios. The maximum detection probability was 15% at 4 min after tsunami occurrence and increased to 80% at 7 min, which corresponds to 9 min before tsunami arrival at the coast. The 80% detection probability line located 3 km behind the tsunami wavefront proceeded to the coast as the tsunami propagated to the coast. To obtain a comprehensive understanding of the tsunami detection probability of the radar system, virtual tsunami observation experiments are required for other seasons in 2014, when the sea surface state was different from that in February, and for other earthquakes.

Keywords: HF radar; tsunami detection; virtual tsunami observation experiment

1. Introduction

High-frequency oceanographic radar (HF radar) is a remote sensing instrument for measuring the ocean current velocity and wave height on the sea surface. HF radar can provide increased spatial and temporal resolution of surface current velocity measurements for important ecological, economic, and safety applications, compared to conventional measurements, such as by GPS wave gages and sea bottom pressure sensors (e.g., [1,2]). Based on a multiyear analysis of HF radar observations off the US west coast, Kim et al. [3] reported continuous surface ocean variability ranging from submesoscale (O(1 km)) to mesoscale (O(1000 km)) and revealed that the spectra decayed with k^{-2} at high wavenumbers, in agreement with theoretical submesoscale spectra. Lipa et al. [4] revealed

periodic time oscillations in the wave parameters (height, period, direction) forced by semidiurnal tides, which was never observed before HF radar. Recently, Lorente et al. [5] demonstrated the significant advantages of HF radar in surface wave measurements, with moderate root mean squared error and correlation coefficients, based on comparisons between HF radar and in situ wave observations during a winter season including extreme wave height events (significant wave height > 10 m). HF radar application for tsunami detection has been discussed theoretically and numerically over the past 40 years (e.g., [6,7]), and since the velocity fields of a tsunami were first measured using HF radar (e.g., [8–10]), the development of HF radar systems for tsunami detection has progressed.

A tsunami arrival detection method based on HF radar-derived radial velocities averaged over an area band parallel to the coastline was first proposed by Lipa et al. [11], and was applied to the actual tsunamis induced by the Tohoku-Oki earthquake [12], and by an earthquake that occurred on 11 April 2012 in Indonesia [13]. The Japan tsunami was detected 15–19 min before its arrival at the coast. Grilii et al. [14] and Guérin et al. [15] proposed a detection method using cross-correlation of the signals received at two points along a tsunami wave ray calculated beforehand and reported detection beyond the continental shelf based on numerical experiments for far- and near-field tsunamis. These previous studies focused on tsunami arrival detection offshore rather than tsunami velocity measurement.

The first warning of the tsunami induced by the 2011 Tohoku-Oki earthquake was issued three minutes after the earthquake. The warning underestimated the tsunami height due to the saturation of magnitude calculated by the seismic data for events of $M_w > 8$, which eventually led to greater tsunami damage [16]. Therefore, in addition to tsunami arrival detection offshore, measured information on the tsunami height offshore is crucial for the mitigation of tsunami disasters. HF radar could improve the tsunami warning system by detecting an approaching tsunami and measuring the tsunami-induced velocities, which can be converted to tsunami height offshore with increased time and space resolution.

The accuracy of tsunami velocity measurement, as well as the tsunami detection performance, are strongly affected by the sea surface state and background noise (BGN) [17]. Therefore, the methods used should be statistically assessed by using actual tsunami observations under various conditions of the sea surface and BGN. However, only two tsunamis (excluding meteotsunamis) have been observed by HF radar so far, namely, the 2011 Japan and 2012 Indonesian tsunamis. To overcome the lack of data, Fuji et al. [18] proposed a virtual tsunami observation experiment inspired by Gurgel et al. [19], where virtual radial tsunami velocity data with actual background noise was generated by synthesizing a simulated tsunami signal and actual signals received by the Nagano Japan Radio Co., Ltd. (NJRC) radar system installed on the coast of Wakayama Prefecture, Japan. They demonstrated the results for a M_w 9.0 Nankai Trough earthquake (Japan Cabinet Office's fault model case 3) that occurred at 00:00 on 5 April 2014. The tsunami detection performance of the NJRC radar system was examined based on the temporal change in the cross-correlation of radial velocities between two observation points along a single beam at "60 min" before and after tsunami arrival. Applying their method and using one-month observation signals received in February 2014, the probability distribution of tsunami detection with respect to the distance from the shore was calculated by Fuji and Hinata [17]. They also discussed the applicability of the HF radar measurement to tsunami height prediction near the coast by comparing the tsunami heights calculated from the offshore radial tsunami velocity measurements and the Japan Meteorological Agency (JMA) tsunami warning category.

Fuji and Hinata [17] examined the tsunami detection performance along a beam by using the cross-correlation obtained 60 min after the earthquake, based on virtual tsunami observation experiments. They used a 60-min moving average to decompose the virtually observed radial velocities into the tsunami and background current velocity components, resulting in an underestimation of the radial tsunami velocity. In the present study, by improving the method proposed by Fuji and Hinata [17] (hereafter referred to as the FH method), we propose a real-time tsunami detection method using a new, simple radial tsunami velocity extraction method, in which to extract the tsunami velocity in real time and to reduce the underestimation, we calculated the tidal current and the residual

current using harmonic analysis and a 60-min average, respectively (see Section 3). In addition, the present method was applied to 12 beams of the radar and its performance was assessed spatially and statistically based on virtual tsunami observation experiments referring to Fuji and Hinata [17].

2. Tsunami Simulation

We simulated tsunami velocities induced by a M_w 9.0 Nankai Trough earthquake. To calculate the tsunami velocity in shallow water, the model used the nonlinear long-wave equation and continuity equation as the fundamental equation:

$$\frac{dM}{dt} + \frac{\partial}{\partial x}\left(\frac{M^2}{h}\right) + \frac{\partial}{\partial x}\left(\frac{MN}{h}\right) + gh\frac{\partial \eta}{\partial x} + \frac{gn^2}{D^{\frac{7}{3}}}M\sqrt{M^2+N^2} = 0, \quad (1)$$

$$\frac{dN}{dt} + \frac{\partial}{\partial y}\left(\frac{MN}{h}\right) + \frac{\partial}{\partial y}\left(\frac{N^2}{h}\right) + gh\frac{\partial \eta}{\partial y} + \frac{gn^2}{D^{\frac{7}{3}}}N\sqrt{M^2+N^2} = 0, \quad (2)$$

$$\frac{dN}{dt} + \frac{\partial}{\partial y}\left(\frac{MN}{h}\right) + \frac{\partial}{\partial y}\left(\frac{N^2}{h}\right) + gh\frac{\partial \eta}{\partial y} + \frac{gn^2}{D^{\frac{7}{3}}}N\sqrt{M^2+N^2} = 0, \quad (3)$$

where η is the water level, g is the acceleration due to gravity, M and N are the flow flux in the east-west and north-south directions, respectively, n is Manning's coefficient of roughness, which is set as 0.025, and h is the water depth. The grid resolution is 1 km in both the east-west and north-south directions, and the calculation time step is 0.5 s. In this simulation, we used the Japan Cabinet Office's fault model case 3 for the Nankai Trough earthquake, which is the same case as that used in Fuji et al. [18] and Fuji and Hinata [17]. Figure 1b shows the tsunami initial sea surface elevation calculated by Okada's formula [20]. We calculated the tsunami velocity field for 48 h after the earthquake, in which background currents (BGCs; e.g., tidal, wind-driven, Kuroshio currents) were not included. The first wave propagating into the Kii Channel has a dominant period of about 60 min. Figure 2 shows the temporal evolution of tsunami wave propagation in and around the Kii Channel at 1, 4, 7, 10, 13, and 16 min after the tsunami.

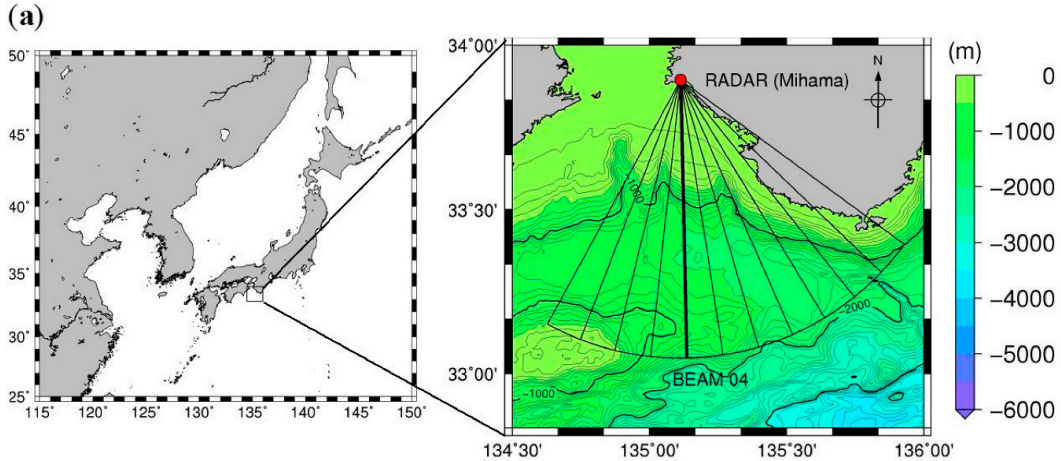

Figure 1. *Cont.*

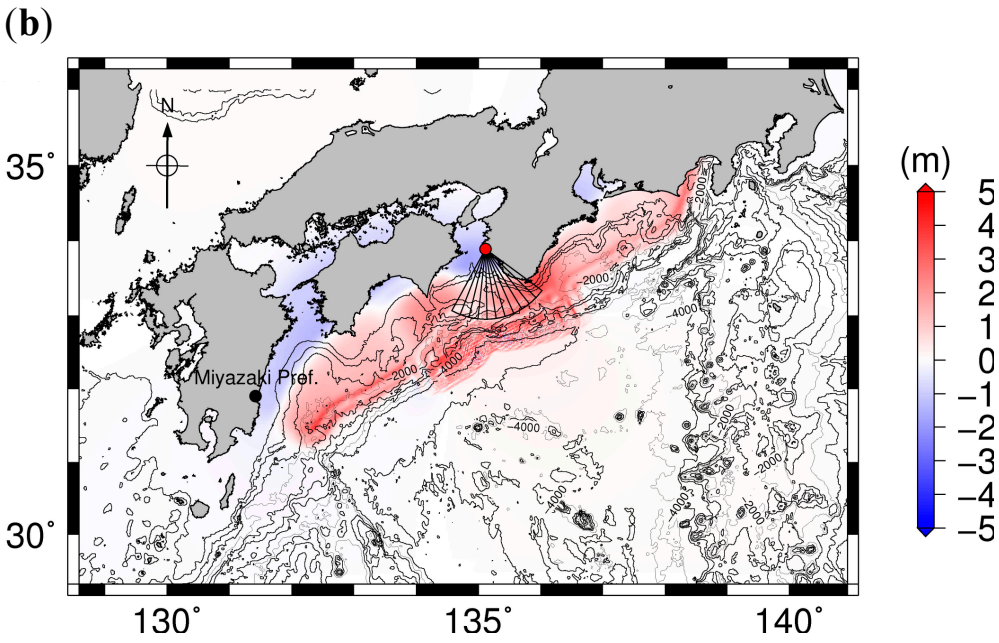

Figure 1. (**a**) Observation area of the high-frequency (HF) radar installed on the Mihama coast and the depth contours of the Kii channel. The red circle represents the radar station; (**b**) initial sea surface elevation of the tsunami induced by the Japan Cabinet Office's fault model case 3.

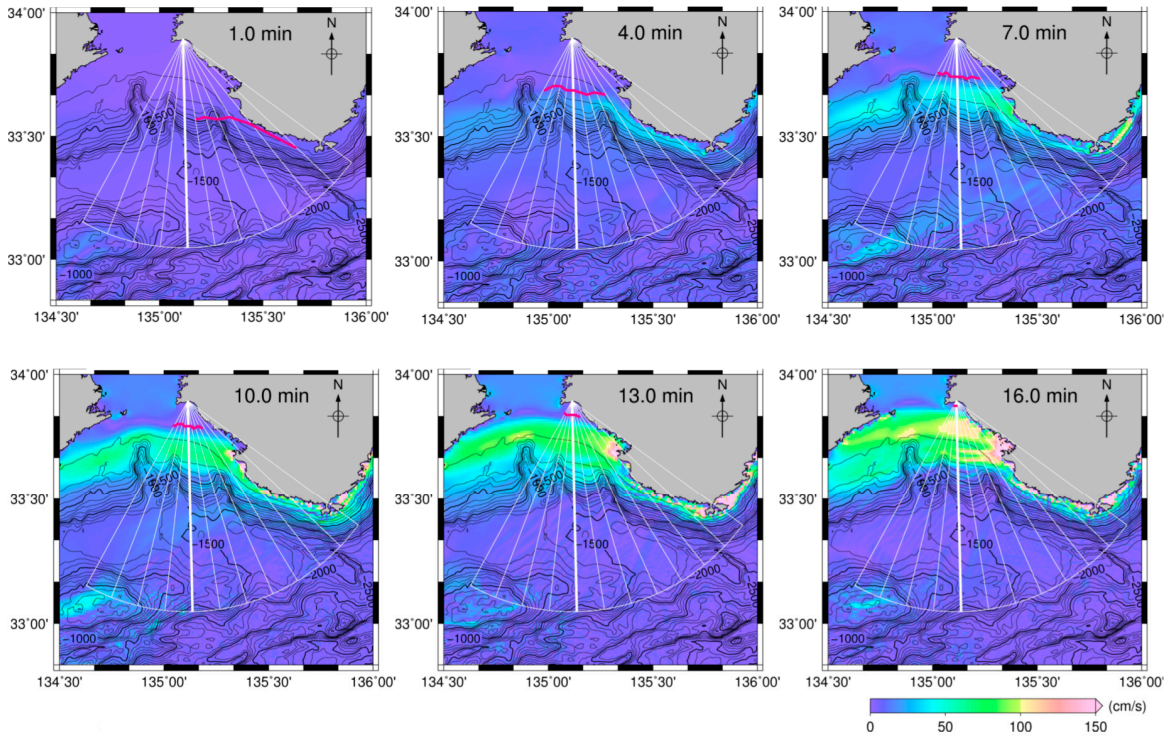

Figure 2. Simulated tsunami propagation within the Kii Channel at 1, 4, 7, 10, 13, and 16 min after tsunami occurrence. The pink line represents the first leading wavefront of the tsunami, defined as the range in which the sea surface slope along the beams calculated from the simulated tsunami heights first exceeds 0.0001.

3. Virtual Tsunami Observation Experiments

3.1. Synthesis of Virtual Observation Signals

We used actual signals received by the NJRC radar obtained during February 2014, as in Fuji and Hinata [17]. The center frequency of the transmitting wave of the radar is 24.515 MHz, the number of beams is 12, sweep bandwidth is 100 kHz, frequency sweep interval is 0.5 s, range resolution is 1.5 km, and there are 64 range cells on each beam. In a normal observation mode with an integration time of, for example, 15 min, analysis is generally performed on the radial velocities obtained in range cells 3–35. The radar system is configured with one transmitting and eight receiving antennas (three-element Yagi). The digital beamforming technique realized a bearing resolution of 7.5° in the angular region of ±45° from the broadside direction. The beam width (half-power) ranged from 13° in the direction of 0° (broadside) to 17.5° in the direction of ±45°. The windowing technique was employed to reduce the side lobes in the radiation pattern: 0 dB for receiving antennas 4 and 5 (Ant 4 and Ant 5); −1 dB for Ant 3 and Ant 6; −2 dB for Ant 2 and Ant 7; and −3 dB for Ant 1 and Ant 8. Here, we used the receiving signals from +45° to −37.5° to produce the synthesized signals described below.

In the tsunami observation mode, the system calculates the sea surface velocities every 1 min from the receiving signals in parallel with the continuous transmission of signals. The HF radar observation area with the depth contours of the Kii Channel is shown in Figure 1a. In this area, the water depth basically becomes deeper with increasing distance offshore from the radar location along every beam and, for example, the continental shelf edge is located at around 30 km offshore along beam 04 (solid line in Figure 1a), which is pointing approximately south.

We created the ideal receiving signals at the range cells that were modulated by the tsunami velocities, as shown below [19]:

$$\Theta(b,m,t) = a_x \exp\left(2\pi j \int_0^t f_{\mathrm{tsu}}(b,m,t)dt\right) \tag{4}$$

$$f_{\mathrm{tsu}}(b,m,t) = 2f_0 v_{\mathrm{tsu}}(b,m,t)/c \tag{5}$$

where b is the beam number (b = 00, 01, . . . , 11), m is the cell number (m = 1, . . . , 64), $v_{\mathrm{tsu}}(b,m,t)$ is the radial tsunami velocity having a dominant period of about 60 min, f_{tsu} is the additional Doppler frequency shift due to $v_{\mathrm{tsu}}(b,m,t)$, j is an imaginary unit, f_0 is the transmission frequency of the HF radar, c is the propagation speed of the radio waves, and the arbitrary amplitude $a_x = 1$. We synthesized receiving signals ($X(b,m,t)$) that would have been received by the HF radar if the tsunami had occurred at a certain time in February 2014 by calculating the Hadamard product of the actual receiving signals ($S(b,m,t)$) and the ideal signals, as follows [17]:

$$X(b,m,t) = S(b,m,t) * \Theta(b,m,t) \tag{6}$$

Here, we calculated $v_{\mathrm{tsu}}(b,m,t)$ by simple linear interpolation of the simulated velocities. In actuality, however, HF radar measurement of the radial velocity would be affected by the inhomogeneity of radar cross sections on the ocean surface in the range cell and also by the beam width, which is narrow in the broadside direction, as mentioned above. In addition, the tsunami waves could break due to shoaling in a shallower region. It is noted that these effects on the radial tsunami velocities have not been considered in this study.

Changing the timing of tsunami occurrence every 1 h from 06:00 on 1 February 2014 to 17:00 on 28 February 2014, synthesized signals of 660 tsunami event scenarios were prepared as in Fuji and Hinata [17]. We then calculated the Doppler spectra from the synthesized signals at 64 range cells on all beams every 1 min by performing a 256-sample (128 s) Fast Fourier Transform overlapping by 128 samples (64 s), resulting in a radial velocity resolution of 4.78 cm/s. The synthesized data are

available on the Institutional Repository website (http://iyokan.lib.ehime-u.ac.jp/dspace/handle/iyokan/5595).

We next calculated the observed and synthesized radial velocities ($v_{obs}(b,m,t), v_{vt}(b,m,t)$) from the corresponding Doppler spectra every 1 min, where t is the time in minutes. In all the scenarios, $v_{vt}(b,m,t)$ was prepared for the period from 6 h before to 6 h after the earthquake. The radial velocities can be decomposed as:

$$\begin{aligned} v_{obs}(b,m,t) &= v_{BGC}(b,m,t) + v_{err}(b,m,t) \\ &= v_{tid}(b,m,t) + v_{res}(b,m,t) + v_{err}(b,m,t) \end{aligned} \tag{7}$$

$$\begin{aligned} v_{vt}(b,m,t) &= v_{BGC}(b,m,t) + v_{tsu}(b,m,t) + v_{err}(b,m,t) \\ &= v_{tid}(b,m,t) + v_{res}(b,m,t) + v_{tsu}(b,m,t) + v_{err}(b,m,t) \end{aligned} \tag{8}$$

where $v_{BGC}(b,m,t)$ represents the BGC components, composed of the tidal current ($v_{tid}(b,m,t)$), residual current ($v_{res}(b,m,t)$), and error velocity $v_{err}(b,m,t)$ caused by various noises, and would also include short-period current velocities likely induced by impulsive wind forcing. $v_{res}(b,m,t)$ has a much longer time scale compared to the tsunami and tidal currents (e.g., wind-driven, density-driven, and Kuroshio currents).

3.2. Real-Time Extraction of Tsunami Velocity Component

Fuji and Hinata [17] extracted the tsunami velocity component from the synthesized radial velocities $v_{vt}(b,m,t)$ by using a 60-min moving average, which resulted in an underestimation of the tsunami velocity (Figure 9 in Fuji and Hinata [17]) because of the overestimation of the longer period (background current) component. Here, we used a new, simple extraction method to reduce the underestimation.

First, we calculated the harmonic constants of four major tidal current components (M2, S2, K1, O1) by harmonic analysis based on the actual radial velocities obtained from February to May 2015 and detided $v_{vt}(b,m,t)$. Let $V(b,m,t)$ be the detided radial velocity, given by:

$$V(b,m,t) = v_{vt}(b,m,t) - v_{tid}(b,m,t) = v_{res}(b,m,t) + v_{tsu}(b,m,t) + v_{err}(b,m,t). \tag{9}$$

Since the residual current component has a much longer time scale compared to the tsunami and error velocities, it can be approximated by:

$$v_{res}(b,m,t_0) \approx \overline{V_0} = \frac{\sum_{t_0-60}^{t_0} V(b,m,t)}{60} \tag{10}$$

where t_0 is the time of tsunami occurrence. Hence,

$$v'_{vt}(b,m,t) = V(b,m,t) - \overline{V_0} \approx v_{tsu}(b,m,t) + v_{err}(b,m,t) \tag{11}$$

$$v'_{obs}(b,m,t) = v_{obs}(b,m,t) - v_{tid}(b,m,t) - \overline{V_0} \approx v_{err}(b,m,t) \tag{12}$$

It should be noted that the first tsunami wave has a dominant period of about 60 min, and that these approximations hold in $t_0 - \Delta t \ll t \ll t_0 + \Delta t$, where Δt is the dominant time scale of the residual currents. In this study, we consider $v'_{vt}(b,m,t)$ as the radial tsunami velocity component including the error velocity mainly depending on the sea surface state [17] and likely on impulsive wind forcing as well. However, since we could not deploy other current meters, such as an acoustic Doppler profiler, to measure the short-period (<60 min) wind-induced current velocity, here we discuss the effects of the sea surface state, that is, the surface wave height, on the tsunami detection performance and measurement accuracy.

3.3. Real-Time Tsunami Detection Method

The detailed procedure of the tsunami wavefront detection method is as described below:

1. Two cross-correlations of radial velocities between two different range cells ($cor_{\mathrm{obs}}(b,m,t)$, $cor_{\mathrm{vt}}(b,m,t)$) were calculated every 1 min from the combinations of $(v'_{\mathrm{obs}}(b,m,t), v'_{\mathrm{obs}}(b,m+2,t))$ and $(v'_{\mathrm{vt}}(b,m,t), v'_{\mathrm{vt}}(b,m+2,t))$ observed in the period of $[t-30, t]$. Specifically, $cor_{\mathrm{obs}}(b,m,t)$ was calculated from 00:30 on 1 February 2014 to 23:59 on 28 February 2014, and $cor_{\mathrm{vt}}(b,m,t)$ was calculated for the duration $[t_0-360, t_0+360]$ in each tsunami event, where t_0 is the time of tsunami occurrence;
2. Frequency distribution of the cross-correlation ($P[cor_{\mathrm{obs}}(b,m,t)]$) in the non-tsunami condition was approximated by a normal distribution;
3. When $cor_{\mathrm{vt}}(b,m,t)$ became larger than the top 1% value of $P[cor_{\mathrm{obs}}(b,m,t)]$ after tsunami occurrence, the significance function $F(b,m)$ was set to 1; otherwise $F(b,m)$ was set to 0;
4. Finally, tsunami arrival was judged by using the tsunami detection factor $TD(b,m)$ defined by Fuji and Hinata [17]:

$$TD(b,m) = F(b,m)\cdot F(b,m+1)\cdot F(b,m+2) \tag{13}$$

$$\begin{cases} TD(b,m) = 0 : \text{no tsunami arrival} \\ TD(b,m) = 1 : \text{tsunami arrival} \end{cases} \tag{14}$$

In summary, to extract the radial tsunami velocity in real time and to reduce the underestimation of the FH method, we detided the synthesized radial velocities using harmonic analysis and estimated the residual current velocity using a 60-min average, whereas Fuji and Hinata [17] used a 60-min moving average to extract the radial tsunami velocity. In addition, the present method was applied to 12 beams of the radar and its performance was assessed statistically, while Fuji and Hinata [17] demonstrated the detection performance (not in real time) only along beam 04.

4. Results and Discussion

4.1. Comparison of Extracted Tsunami Velocities

We validated the present tsunami extraction method (3.2) by comparing the extracted velocities by the present method and those by the FH method. Figure 3 shows examples of temporal variations of the simulated radial tsunami velocity ($v_{\mathrm{tsu}}(b,m,t)$; black line) and extracted tsunami velocities by the present method ($v'_{\mathrm{vt}}(b,m,t)$; red line) and by the FH method (blue line) at range cell 10 on beam 04 for the scenarios in which the tsunami occurred at (**a**) 06:00 on 1 February 2014 (hereafter referred to as the 02010600 scenario) and at (**b**) 13:00 on 27 February 2014 (hereafter referred to as the 02271300 scenario) when the significant wave height was over 5 m. In Figure 3a, the FH method consistently underestimated the radial tsunami velocity by 10–20 cm/s, which corresponds to 0.29–0.58 m in wave height at the range cell, while the radial tsunami velocity extracted by the present method almost coincides with the simulated radial velocity, and the underestimation of the second peak of the first tsunami wave is less than 10 cm/s. This relationship between the three velocities holds in Figure 3b, except at 13:19 on 27 February, when both of the extracted velocities were larger than the simulated radial velocity. This was due to the poorer S/N ratio caused by higher surface wind waves on 27 February [17].

Figures 4 and 5 show the spatial distributions of the extraction errors, namely, the differences between the simulated radial velocity and the extracted radial tsunami velocities by the present method (**a**–**c**) and by the FH method (**d**–**f**) at 7, 10, and 13 min after tsunami occurrence. The tsunami velocity extracted by the FH method was consistently underestimated over the entire continental shelf within a 30-cell range from the radar in both scenarios. On 27 February, even larger errors appeared on the shelf due to the even poorer S/N ratio caused by even larger surface wave heights.

However, as a whole, the underestimation was reduced by the present method, which was confirmed by 28 scenarios in which the tsunami occurred at 06:00 on each day of February 2014.

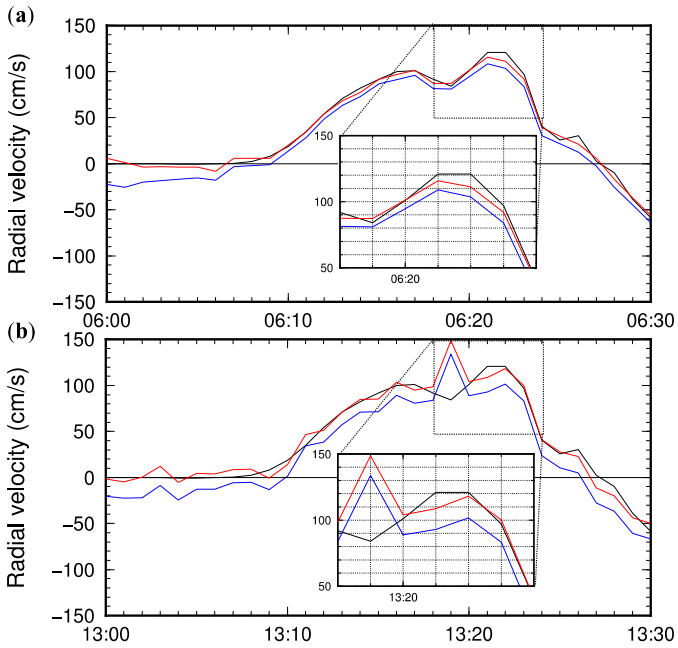

Figure 3. Comparison of temporal variations of simulated radial tsunami velocity ($v_{\mathrm{tsu}}(04, 10, t)$; black line) and extracted tsunami velocities at range cell 10 on beam 04 by the present method ($v'_{\mathrm{vt}}(04, 10, t)$; red line) and by the Fuji and Hinata (FH) method (blue line) for scenarios in which the tsunami occurred at (**a**) 06:00 on 1 February 2014 and (**b**) 13:00 on 27 February 2014.

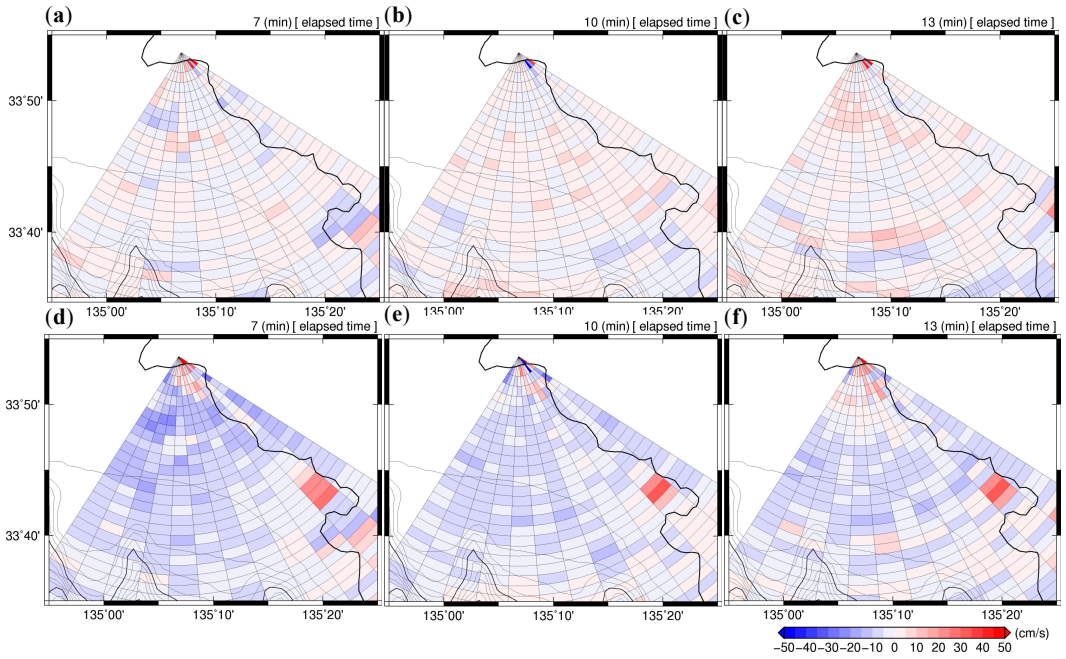

Figure 4. Spatial distributions of the differences between the simulated radial velocity and the extracted radial tsunami velocities by the present method (**a**–**c**) and by Fuji and Hinata (FH) method (**d**–**f**) for the 02010600 scenario. The background color represents the velocity difference between the two kinds of velocities.

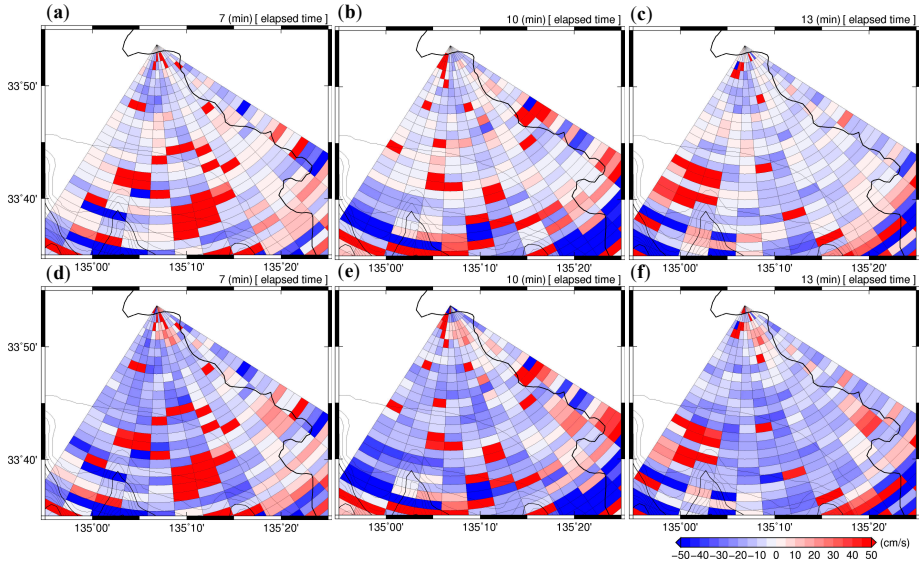

Figure 5. Same as Figure 4, but for the 02271300 scenario.

Figure 6 shows the average errors and root mean squared errors (RMSEs) of the maximum positive velocities induced by the first tsunami wave (**a**) at each range cell extracted by the present method (**b**,**c**) and by the FH method (**d**,**e**) calculated from the 28 scenarios. On the shelf, with the present method, the errors and RMSEs were within ±10 cm/s and smaller than 15 cm/s, respectively, while the FH method consistently underestimated the maximum velocity by about 10–30 cm/s with larger RMSEs of 10–30 cm/s. However, on and beyond the shelf slope, the errors and RMSEs were not significantly different between the two methods, since much smaller tsunami velocities were induced in the region due to deeper water depths. As pointed out in the Introduction, quantitative information on tsunamis (velocity, height) is crucial for improving the JMA tsunami warning issued 3 min after an earthquake. Based on these comparisons, the present method effectively avoids underestimation of the tsunami magnitude.

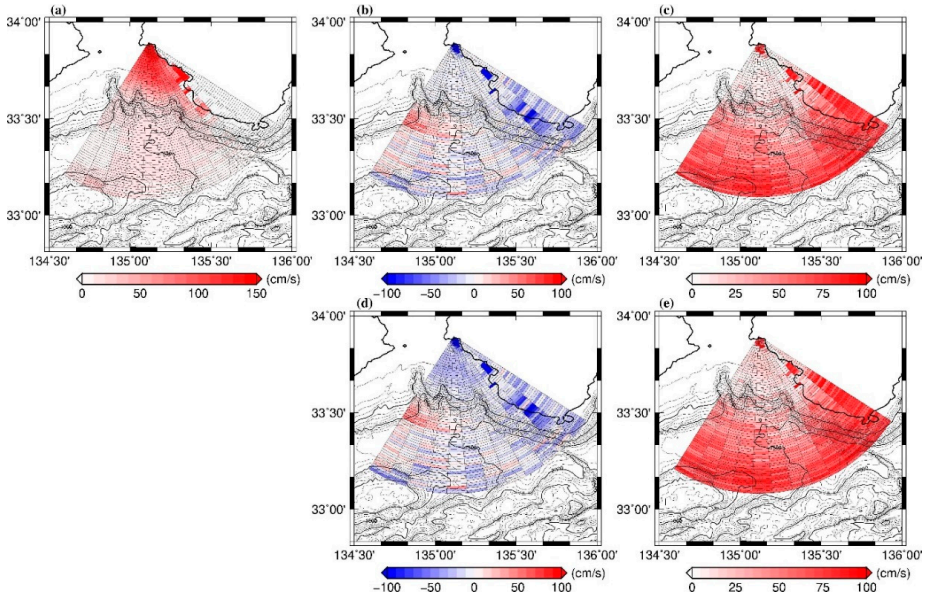

Figure 6. Maximum positive radial velocities induced by the first tsunami wave (**a**). Extraction errors of the maximum velocities by the present method (**b**,**c**) and the FH method (**d**,**e**). Average errors of 28 scenarios (**b**,**d**) and root mean squared errors (RMSEs) (**c**,**d**).

4.2. Real-Time Tsunami Detection for 02010600 and 02271300 Scenarios

As the first step, we applied the present tsunami detection method to beam 04 for a scenario in which the tsunami occurred at 06:00 on 1 February 2014 (02010600 scenario). Figure 7a shows a time-distance diagram of the extracted $v'_{\mathrm{vt}}(04, m, t)$ superimposed with the detection results from Equation (14). The green circles represent the time, $t_{\mathrm{d}}(04, m)$, when the tsunami was detected ($TD(b, m) = 1$), and the black line represents the arrival time of the first leading wavefront of the tsunami, ($t_{\mathrm{a}}(04, m)$), empirically defined as the time when the sea surface slope along the beam calculated from the simulated tsunami heights first exceeds 0.0001. The diagram demonstrates that the tsunami was first detected at a distance of 31.5 km (range cell: 21) from the coast 5 min after tsunami occurrence. Namely, it would have been possible to provide information on the approaching tsunami about 11 min before the tsunami arrival at the radar site. The time-lag, ($t_{\mathrm{lag}}(04, m)$), between $t_{\mathrm{d}}(04, m)$ and $t_{\mathrm{a}}(04, m)$ was consistently about 4 min on the shelf ($m \leq 20$), while the time-lag, $t_{\mathrm{lag}}(04, m)$, increased with increasing distance offshore from 33 km ($m \geq 22$) on the shelf slope. For practical purposes, the tsunami would not have been detected beyond 36 km ($m \geq 24$) in this scenario.

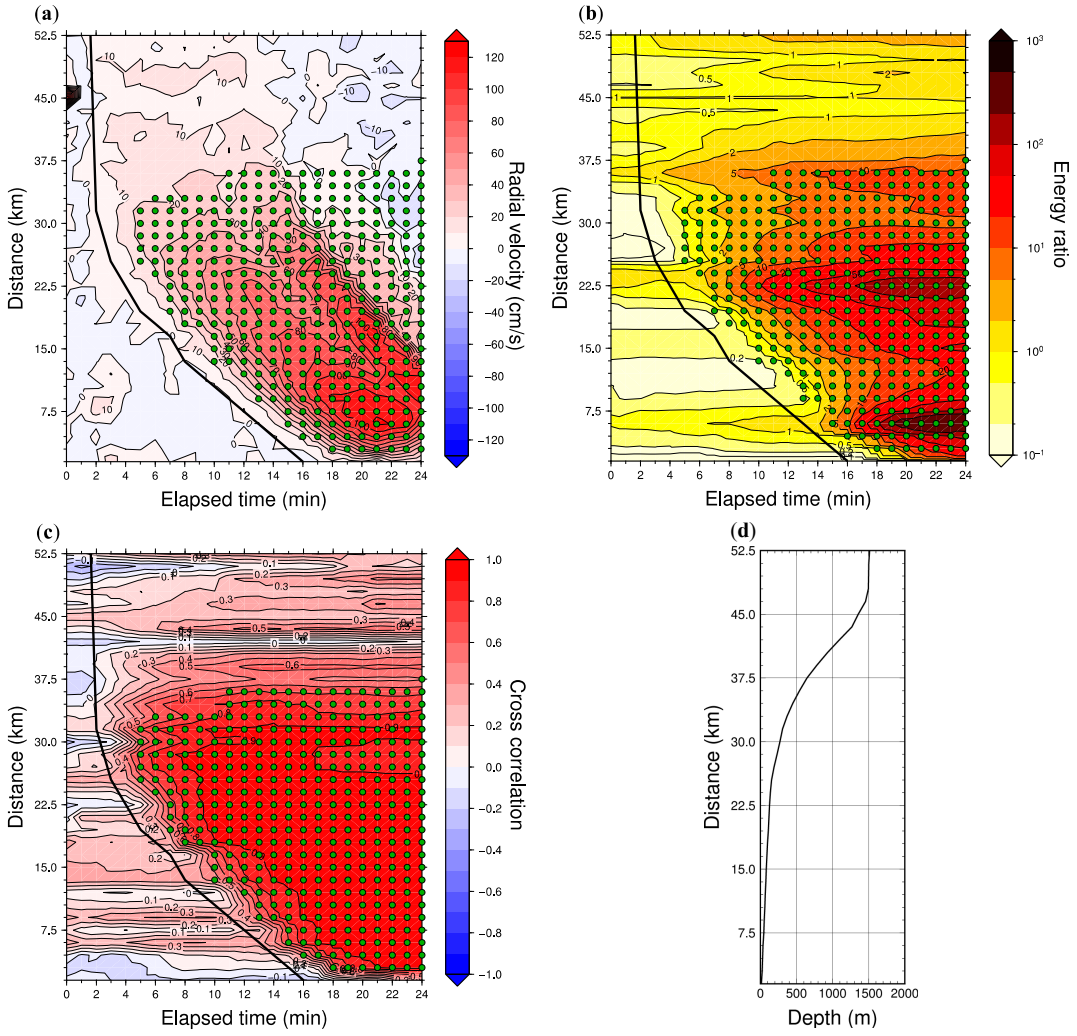

Figure 7. Time-distance diagrams of (**a**) $v'_{\mathrm{vt}}(04, m, t)$, (**b**) $E_{\mathrm{ratio}}(04, m, t)$, (**c**) $cor_{\mathrm{vt}}(04, m, t)$, and detection results along beam 04 for the 02010600 scenario. Green circles represent the time, $t_{\mathrm{d}}(04, m)$, when the tsunami was detected, ($TD(b, m) = 1$), and the black line represents the track of the first leading wavefront of the tsunami. (**d**) Water depth along the beam.

According to Fuji and Hinata [17], the cross-correlation is primarily related to the kinetic energy ratio between $v_{\mathrm{tsu}}(b,m,t)$ and $v'_{\mathrm{obs}}(b,m,t)$, represented by:

$$cor_{\mathrm{vt}}(b,m,t_n) \approx \frac{\sum_{k=n-30}^{n} v^2{}_{\mathrm{tsu}}(b,m,t_k)}{\sum_{k=n-30}^{n}(v'^2{}_{\mathrm{obs}}(b,m,t_k)+v^2{}_{\mathrm{tsu}}(b,m,t_k))} = \frac{1}{\frac{1}{E_{\mathrm{ratio}}(b,m,t_k)}+1} \quad (15)$$

$$E_{\mathrm{ratio}}(b,m,t_n) = \frac{\sum_{k=n-30}^{n} v^2{}_{\mathrm{tsu}}(b,m,t_k)}{\sum_{k=n-30}^{n} v'^2{}_{\mathrm{obs}}(b,m,t_k)} \quad (16)$$

where n is the elapsed time in minutes after tsunami occurrence. Focusing on the relationship between $E_{\mathrm{ratio}}(04,m,t)$ and the detectability of the tsunami, it can be seen from Figure 7b that the tsunami was detected when $E_{\mathrm{ratio}}(04,m,t) \geq 0.5$ on the shelf and ≥ 5 on the slope. On the shelf ($m \leq 20$), $E_{\mathrm{ratio}}(04,m,t)$ increased rapidly to a value between 10^0 and 10^1 after the wavefront arrival, because the kinetic energy of $v'_{\mathrm{tsu}}(04,m,t)$ was comparatively larger due to the shallower water depth and $v'_{\mathrm{obs}}(04,m,t)$ ($\approx v_{\mathrm{err}}(b,m,t)$) was comparatively smaller due to the shorter distance from the radar. On the other hand, on the shelf slope ($m \geq 21$), $E_{\mathrm{ratio}}(b,m,t)$ increased slowly with respect to time because the kinetic energy of $v'_{\mathrm{tsu}}(04,m,t)$ was smaller due to the larger water depth and, in addition, $v'_{\mathrm{obs}}(04,m,t)$ ($\approx v_{\mathrm{err}}(b,m,t)$) was larger due to the poorer S/N ratio at the longer distance from the radar.

The time-distance diagram of $cor_{\mathrm{vt}}(04,m,t)m$, shown in Figure 7c, indicates that the cross-correlation, ($cor_{\mathrm{vt}}(04,m,t)$), took time to increase. In addition, a slightly larger cross-correlation value is required for tsunami detection on the slope: The tsunami was first detected at the time when $cor_{\mathrm{vt}}(04,m,t)$ became 0.4–0.6 on the shelf, but 0.6–0.8 on the slope. This is partly due to the wider distributions of the cross-correlation ($P[cor_{\mathrm{obs}}(b,m,t)]$) on the shelf slope: The top 1% value is 0.516 at $m = 10$ on the shelf, while it is 0.625 at $m = 35$ on the slope.

The tsunami was spatially detected by applying the procedure to all the beams. Figure 8a–f shows the temporal evolution of the detection at 1, 4, 7, 10, 13, and 16 min after tsunami occurrence for the 02010600 scenario superimposed on the extracted tsunami velocity, ($v'_{\mathrm{vt}}(b,m,t)$). The green circle represents the range cell, ($m_{\mathrm{d}}(b,t)$), where the tsunami was detected, ($TD(b,m) = 1$), and the pink line represents the first leading wavefront of the tsunami, the same as in Figure 2. The tsunami was first detected on beams 06–08 on the shelf edge, 4 min after tsunami occurrence. At 7 min, the tsunami was detected on all the beams and then the tsunami-detected range cells extended onshoreward and also slightly offshoreward as the tsunami propagated to the coast at the radar site. The gaps between the onshoremost range cells and the tsunami wavefront ranged between 1.5 and 3.0 km. The offshoremost range cells aligned approximately along the water depth contours of 500–1000 m at 16 min, indicating the dependency of this real-time tsunami detection method on the bottom topography.

Even higher wind waves drastically reduced the tsunami detection performance, even on the continental shelf (Figure 9a–f). For the 02271300 scenario, the tsunami was first detected 10 min after its occurrence only on beam 01 at a water depth of about 150 m. Even at 16 min, the tsunami was hardly detected on the shelf. The gaps between the wavefront and the onshoremost detected cells were even larger than those in the 02010600 scenario. Tsunami detection would have failed in this case because of the poorer S/N ratio [17]. These results demonstrate that the detection method should be statistically evaluated due to the dependency of the detection distance on the time-variant S/N ratio.

4.3. Statistical Evaluation of Real-Time Tsunami Detection

We performed the statistical analysis of the tsunami detection probability using 660 tsunami scenarios: In the first scenario, the tsunami occurred at 6:00 on 1 February; in the second, the tsunami occurred at 7:00 on 1 February; and in the last scenario, the tsunami occurred at 17:00 on 28 February. It is noted that HF radar observation failed in 70/660 scenarios due to intermittent system troubles. Figure 10a–f shows the spatiotemporal evolution of the detection probability at 1, 4, 7, 10, 13, and 16 min

after tsunami occurrence, and the depth contours in and around the Kii Channel. The color represents the detection probability, and the pink line represents the first leading wavefront of the tsunami.

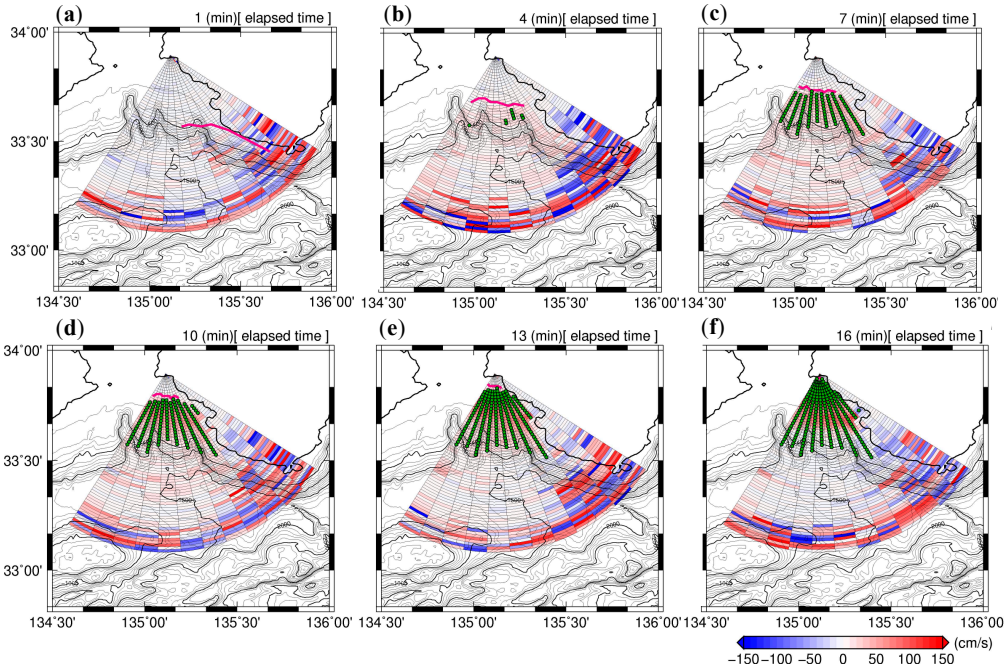

Figure 8. Spatiotemporal evolution of tsunami detection for the 02010600 scenario at (**a**) 1, (**b**) 4, (**c**) 7, (**d**) 10, (**e**) 13, and (**f**) 16 min after tsunami occurrence, and the depth contours of the Kii Channel. The background color represents $v'_{\mathrm{vt}}(b,m,t)$, the green circles represent the tsunami-detected range cells, $m_{\mathrm{d}}(b,t)$, where $TD(b,m) = 1$, and the pink line represents the first leading wavefront of the tsunami.

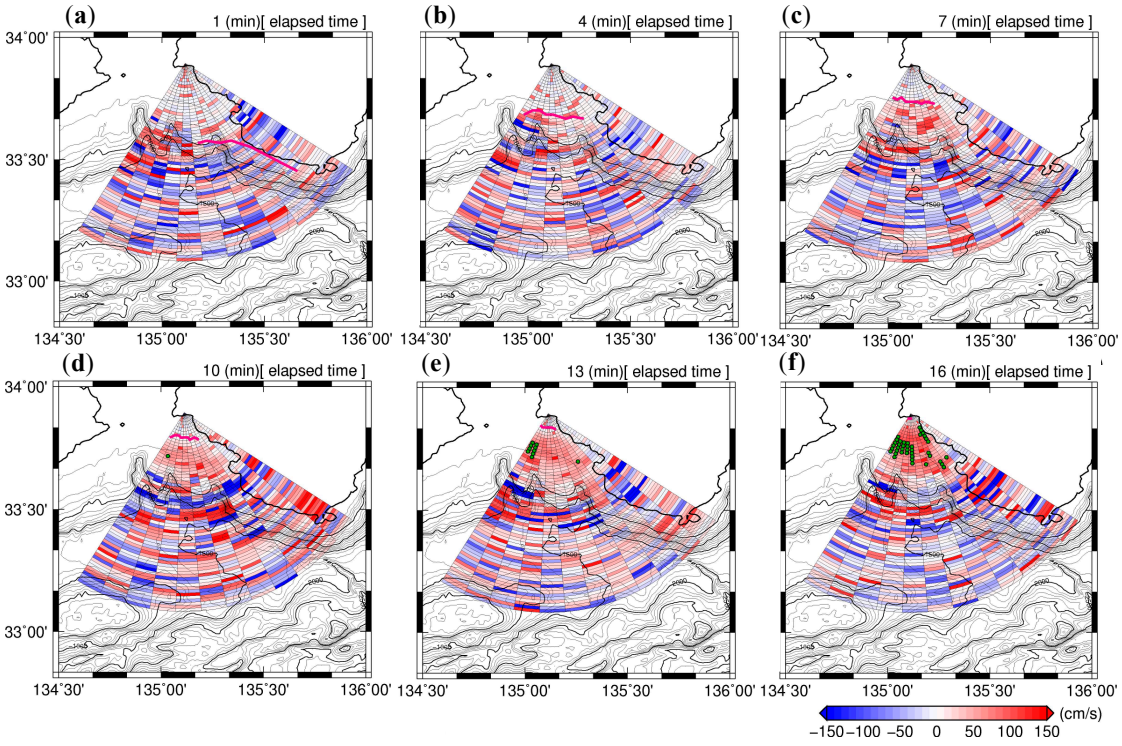

Figure 9. Same as Figure 8, but for the 02271300 scenario.

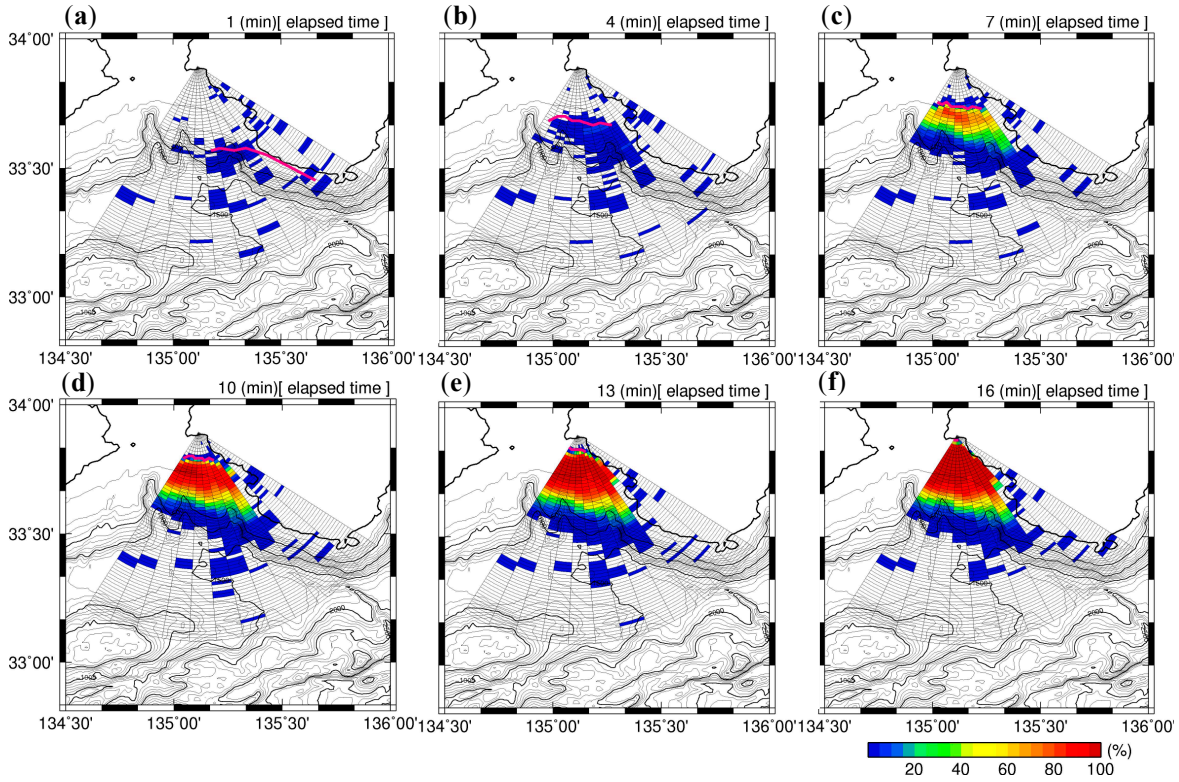

Figure 10. Temporal variations of the detection probability at (**a**) 1, (**b**) 4, (**c**) 7, (**d**) 10, (**e**) 13, and (**f**) 16 min after tsunami occurrence, and the depth contours of the Kii Channel. The background color represents the detection probability, and the pink line represents the first leading wavefront of the tsunami, $m_f(b,t)$.

The maximum detection probability of 15% appeared behind the wavefront along beams 05 and 06 at 4 min and rapidly increased to 80% at 7 min, which corresponds to 9 min before tsunami arrival at the coast. The nearshoremost range cells of 80% detection probability were generally located 3 km behind the wavefront that proceeded to the coast as the tsunami propagated to the coast. Since the detection probability was mostly 0% between the coast and the wavefront, the present method is almost free from misdetection of a tsunami. On the other hand, the detection probability decreased offshoreward from the shelf edge at a water depth of 200 m. On the shelf slope at water depths greater than 500 m, the detection probability was lower than 10%.

Figure 11 shows the temporal evolution of the detection probability at different significant wave height conditions. The result for 1 m$< H_s \leq$ 2 m is not shown here since it is almost the same as for the 0 m $< H_s \leq$ 1 m case. The detection probability clearly depends on the wave height: It gradually decreased as the wave height increased at moderate wave height conditions ($H_s \leq$ 3 m), and significantly decreased when the wave height was larger than 4 m. For practical purposes, tsunami detection by the present method with the NJRC radar system would have failed in 8/590 scenarios in February 2014. These results demonstrate the dependency of tsunami detection on the sea surface state. However, the number of scenarios for even larger wave conditions (e.g., 4 m $< H_s$) is not sufficient for validating the performance of the present method with the NJRC radar system; it is necessary to perform virtual tsunami experiments for other seasons in 2014.

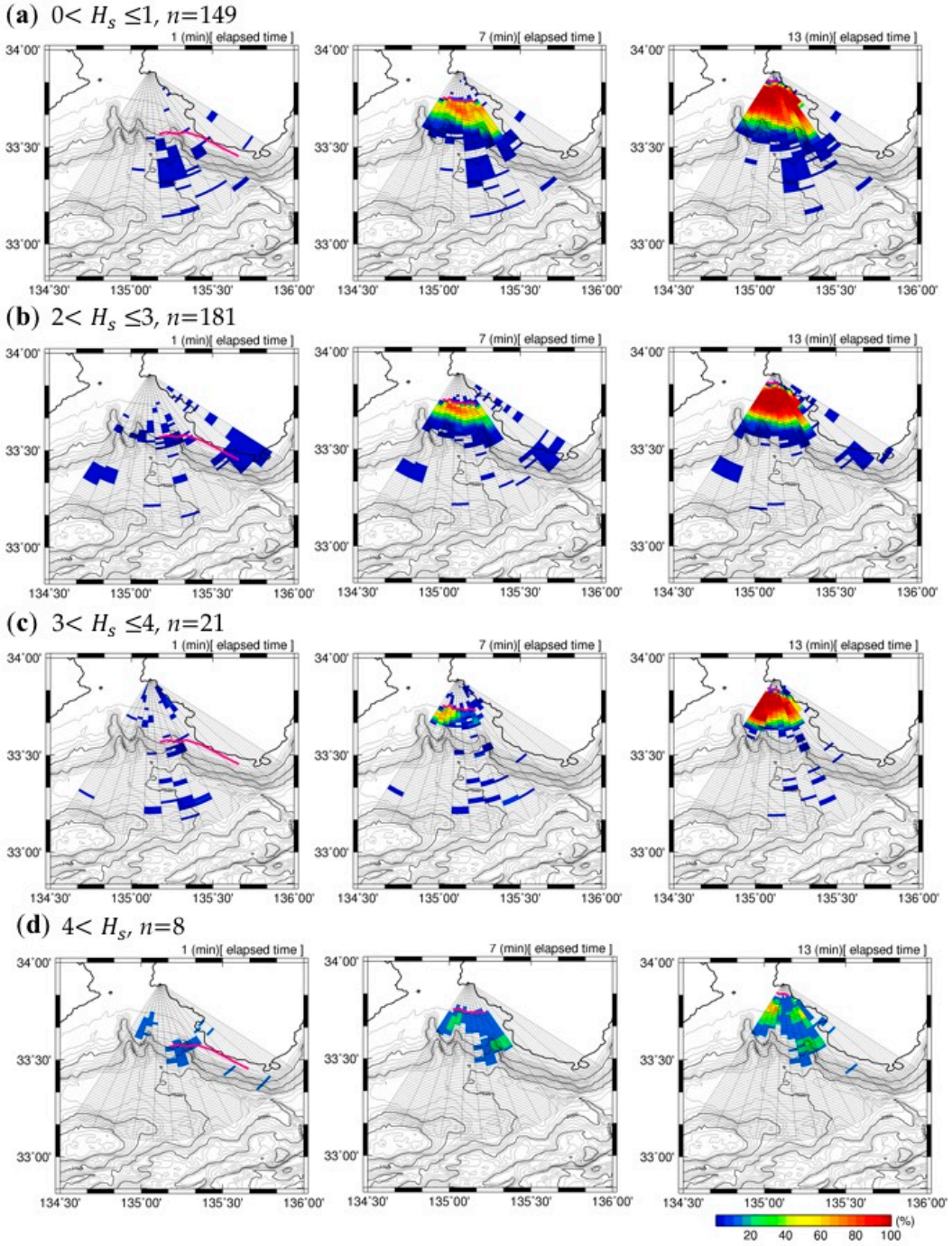

Figure 11. Temporal evolution of the detection probability at 1, 7, and 13 min after tsunami occurrence in different significant wave height (H_s) conditions: (**a**) $0 < H_s \leq 1$, (**b**) $2 < H_s \leq 3$, (**c**) $3 < H_s \leq 4$, and (**d**) $4 < H_s$. The background color represents the detection probability, and the pink line represents the first leading wavefront of the tsunami, $m_f(b, t)$. The wave height is in meters and n represents the number of scenarios used to calculate the probability.

5. Discussion and Conclusions

In this study, we applied a real-time tsunami detection method based on the temporal change in the cross-correlation of radial velocities between two observation points along radar beams, and the performance of the method was statistically evaluated referring to Fuji and Hinata [17]. In the experiments, actual signals received in February 2014 by the NJRC HF radar system installed on

the Mihama coast in Wakayama Prefecture and simulated tsunami velocities induced by the Nankai Trough earthquake (Japan Cabinet Office's fault model case 3) were used and synthesized by the method proposed by Gurgel et al. [19].

Fuji and Hinata [17] extracted the radial tsunami velocity component from the synthesized radial velocities by using a 60-min moving average. However, their method (FH method) raised concerns about the underestimation of the tsunami velocity component. We proposed a new extraction method and validated the method by comparing the radial tsunami velocity components with those extracted by the FH method, and found that the FH method consistently underestimated the tsunami velocity of the first wave by 10–20 cm/s, which corresponds to 0.29–0.58 m in wave height at the comparison point on the continental shelf, while the tsunami velocity extracted by the present method almost coincided with the simulated radial velocity. The first tsunami wave had double peaks in the radial velocity on the continental shelf of the Kii Channel: The radial velocity of the first peak at cell 10 on beam 04 was 100 cm/s; the second peak was 120 cm/s. The extraction errors of the peaks were 1 cm/s for the first peak and less than 10 cm/s for the second peak. The present method is superior to the FH method in terms of relaxing the underestimation of the tsunami magnitude.

In the case in which the earthquake occurred at 6:00 on 1 February 2014, the tsunami would have been detected 31.5 km offshore on the shelf edge at 4 min after its occurrence. On the other hand, if the earthquake had occurred at 13:00 on 27 February 2014, when the significant wave height was over 5 m, tsunami detection would have failed even on the continental shelf because of the poor signal-to-noise ratio [17]. Statistical analysis of the detection probability was performed using 660 tsunami scenarios: The first-scenario tsunami occurred at 6:00 on 1 February; the second occurred at 7:00 on 1 February; and the last occurred at 17:00 on 28 February. HF radar observation failed in 70/660 tsunami scenarios due to intermittent system troubles. The maximum detection probability was 15% at 4 min after tsunami occurrence and increased to 80% at 7 min (9 min before tsunami arrival at the coast). The 80% detection probability line located 3 km behind the first wavefront proceeded to the coast as the tsunami approached the coast.

A tsunami arrival detection method based on HF radar-derived radial velocities averaged over an area band parallel to the coastline and the q-factor was first proposed by Lipa et al. [11], and was applied to the actual tsunamis induced by the Tohoku-Oki earthquake [12], and by an earthquake that occurred on 11 April 2012 in Indonesia [13]. The Japan tsunami was detected 15–19 min before its arrival at the coast. Grilii et al. [14] and Guérin et al. [15] proposed a detection method using cross-correlation of the signals received at two points along a tsunami wave ray calculated beforehand and reported detection beyond the continental shelf, based on numerical experiments for far- and near-field tsunamis. The usage of band-averaged velocities is effective for detecting an incoming tsunami by reducing the observed errors in radial velocities and extracting the coherent motions of surface waters. The receiving-signal-based method effectively detects a tsunami in deeper waters because it does not require inverting currents. On the other hand, there are some difficulties in determining the value of the q-factor beforehand, which varies with the bottom topography and tsunami magnitude, and in applying the method to a region with a complex bottom topography when the area-band-averaged velocities are used for tsunami arrival detection. For the signal-based method, it is necessary to calculate the tsunami wave rays beforehand, and the performance depends on the selection of rays and the choice of low- and high-contrast threshold values (Guérin et al. [15]).

Both current-based and receiving-signal-based methods should be validated and assessed through statistical analysis based on long-term observation signals observed by HF radar over at least a full year for a large variety of oceanic conditions, because their detection performance will vary in accordance with the sea surface state (Guérin et al. [15]; Fuji and Hinata [17]). However, long-term performance assessment of these methods has not yet been fully conducted. For the present method with the NJRC radar system, the detection probability clearly depends on the wave height: It gradually decreased as the wave height increased at moderate wave height conditions ($H_s \leq 3$ m), and significantly decreased

when the wave height was larger than 4 m, although the number of scenarios for even larger wave conditions (e.g., 4 m < H_s) is not sufficient for comprehensively validating the performance.

We have been developing current-based detection methods, because HF radar tsunami measurements are expected to be used not only to detect an approaching tsunami, but also to validate and improve the JMA tsunami warning category (tsunami magnitude) issued 3 min after an earthquake in Japan (Fuji and Hinata [17]). In addition, tsunami velocity measurements can be used as basic information to cancel a tsunami warning in addition to the sea level records measured at tidal stations along the coast, the timing of which is crucial for starting rescue operations and mitigating tsunami damage. To obtain a comprehensive understanding of the tsunami detection probability of the radar system and tsunami measurement accuracy, we will perform virtual tsunami experiments for other seasons in 2014, when the sea surface state was different from that in February, and/or for other earthquakes.

Considering the recent progress in HF radar measurement of wind-wave parameters (e.g., [4,5]), we should be able to evaluate the detection probability along the beams for a tsunami scenario in real time in the near future. In addition, we will soon apply the present method for longer-range NJRC HF radars with a center frequency of 13.5 MHz, to be deployed on the southeast coast of Kyushu Island in Miyazaki Prefecture (see Figure 1) and operated from April 2019. Higher tsunami detection probability on the shelf slope is expected to be achieved by increasing the SNR, or equivalently, increasing the energy ratio (E_{ratio}) due to the decrease in background current energy, (${v'^2}_{\mathrm{obs}}$), including the radial velocity energy error.

Author Contributions: H.H. and T.T. conceived this research. K.O., S.S., and R.F. performed the main data analysis. All authors contributed to the discussion. K.O., S.S., and H.H. wrote and revised manuscript.

Funding: This research was supported by a collaborative research project between Ryukyu University, Ehime University and Kansai University, a collaborative research project between Ehime University and Kokusai Kogyo Co., Ltd., the Mitsubishi Foundation, JSPS Grant-in-Aid for Scientific Research (KAKENHI) No. 16H04419, and MIC/SCOPE Grant No. 165011003.

Acknowledgments: The receiving data of the radar installed at Mihama coast was provided by the National Institute for Land and Infrastructure Management.

Conflicts of Interest: The authors declare no conflict of interest.

References

1. Atan, R.; Goggins, J.; Hartnett, M.; Agostinho, P.; Nash, S. Assessment of wave characteristics and resource variability at a 1/4-scale wave energy test site in Galway Bay using waverider and high frequency radar (CODAR) data. *Ocean Eng.* **2016**, *117*, 272–291. [CrossRef]
2. Falco, P.; Buonocore, B.; Cianelli, D.; De Luca, L.; Giordano, A.; Iermano, I.; Kalampokis, A.; Saviano, S.; Uttieri, M.; Zambardino, G.; et al. Dynamics and sea state in the Gulf of Naples: Potential use of high-frequency radar data in an operational oceanographic context. *J. Oper. Oceanogr.* **2016**, *9*, s33–s45. [CrossRef]
3. Kim, S.Y.; Terrill, E.J.; Cornuelle, B.D.; Jones, B.; Washburn, L.; Moline, M.A.; Paduan, J.D.; Garfield, N.; Largier, J.L.; Crawford, G.; et al. Mapping the U.S. West Coast surface circulation: A multiyear analysis of high-frequency radar observations. *J. Geophys. Res.* **2011**, *116*, C03011. [CrossRef]
4. Lipa, B.; Barrick, D.; Alonso-Martirena, A.; Fernandes, M.; Ferrer, M.I.; Nyden, B. Brahan project high frequency radar ocean measurements: Currents, winds, waves and their interactions. *Remote Sens.* **2014**, *6*, 12094–12117. [CrossRef]
5. Lorente, P.; Sotillo, M.G.; Aouf, L.; Amo-Baladrón, A.; Barrera, E.; Dalphinet, A.; Toledano, C.; Rainaud, R.; De Alfonso, M.; Piedracoba, S.; et al. Extreme Wave Height Events in NW Spain: A Combined Multi-Sensor and Model Approach. *Remote Sens.* **2018**, *10*. [CrossRef]
6. Barrick, D. Theory of HF and VHF propagation across the rough sea, 2, Application to HF and VHF propagation above the sea. *Radio Sci.* **1971**, *6*, 527–533. [CrossRef]
7. Barrick, D. A coastal radar system for tsunami warning. *Remote Sens. Environ.* **1979**, *8*, 353–358. [CrossRef]

8. Hinata, H.; Fujii, S.; Furukawa, K.; Kataoka, T.; Miyata, M.; Kobayashi, T.; Mizutani, M.; Kokai, T.; Kanatsu, N. Propagating tsunami wave and subsequent resonant response signals detected by HF radar in the Kii Channel, Japan. *Estuar. Coast. Shelf Sci.* **2011**, *95*, 268–273. [CrossRef]
9. Lipa, B.; Barrick, D.; Saitoh, S.; Ishikawa, Y.; Awaji, T.; Largier, J.; Garfield, N. Japan tsunami current flows observed by HF radars on two continents. *Remote Sens.* **2011**, *3*, 1663–1679. [CrossRef]
10. Dzvonkovskaya, A. Ocean surface current measurements using HF radar during the 2011 Japan tsunami hitting Chilean coast. In Proceedings of the 2012 IEEE International Geoscience and Remote Sensing Symposium, Munich, Germany, 22–27 July 2012; pp. 7605–7608. [CrossRef]
11. Lipa, B.; Barrick, D.; Bourg, J.; Nyden, B. HF radar detection of tsunamis. *J. Oceanogr.* **2006**, *62*, 705–716. [CrossRef]
12. Lipa, B.; Isaacson, J.; Nyden, B.; Barrick, D. Tsunami arrival detection with high frequency (HF) radar. *Remote Sens.* **2012**, *4*, 1448–1461. [CrossRef]
13. Lipa, B.; Barrick, D.; Diposaptono, S.; Isaacson, J.; Jena, B.K.; Nyden, B.; Rajesh, K.; Kumar, T.S. High frequency (HF) radar detection of the weak 2012 Indonesian tsunamis. *Remote Sens.* **2012**, *4*, 2944–2956. [CrossRef]
14. Grilli, S.T.; Grosdidier, S.; Guerin, C.A. Tsunami detection by high-frequency radar beyond the continental shelf. *Pure Appl. Geophys.* **2016**, *173*, 3895–3934. [CrossRef]
15. Guérin, C.A.; Grilli, S.T.; Moran, P.; Grilli, A.R.; Insua, T.L. Tsunami detection by high-frequency radar in British Columbia: Performance assessment of the time-correlation algorithm for synthetic and real events. *Ocean Dyn.* **2018**, 423–438. [CrossRef]
16. Seto, S.; Takahashi, T. Examination on the observation site of oceanographic radar for tsunami source and propagation in the Nankai trough. *J. Jpn. Soc. Civ. Eng. Ser. B* **2015**, *71*, 343–348. [CrossRef]
17. Fuji, R.; Hinata, H. Temporal variability of tsunami arrival detection distance revealed by virtual tsunami observation experiments using numerical simulation and 1-month HF radar observation. *J. Oceanogr.* **2017**, *73*, 1725–1741. [CrossRef]
18. Fuji, R.; Hinata, H.; Fujii, S.; Nagamatsu, H.; Ogasawara, I.; Ito, H.; Kataoka, T.; Takahashi, T. Tsunami detection based on virtual tsunami observation experiment by using oceanographic radar. *J. Jpn. Soc. Civ. Eng. Ser. B* **2015**, *71*, 337–342. [CrossRef]
19. Gurgel, K.W.; Dzvonkovskaya, A.; Pohlmann, T.; Schlick, T.; Gill, E. Simulation and detection of tsunami signatures in ocean surface currents measured by HF radar. *Ocean Dyn.* **2011**, *61*, 1495–1507. [CrossRef]
20. Okada, Y. Internal deformation due to shear and tensile faults in a half-space. *Bull. Seismol. Soc. Am.* **1992**, *82*, 1018–1040.